

Constraint Learning for Parametric Point Cloud

Xi Cheng¹ Ruiqi Lei¹ Di Huang¹ Zhichao Liao¹ Fengyuan Piao¹ Yan Chen¹
Pingfa Feng^{1,2} Long Zeng^{1,†}

†: Corresponding authors

¹Tsinghua Shenzhen International Graduate School, Tsinghua University, Shenzhen, China

²Department of Mechanical Engineering, Tsinghua University, Beijing, China

{chengxi23, leirq22}@mails.tsinghua.edu.cn, dihuangdylan@gmail.com,

{liaozc23, pfy22, chenyan23}@mails.tsinghua.edu.cn,

fengpf@tsinghua.edu.cn, zenglong@sz.tsinghua.edu.cn

Abstract

Parametric point clouds are sampled from CAD shapes, and have become increasingly prevalent in industrial manufacturing. However, most existing point cloud learning methods focus on the geometric features, such as developing efficient convolution operations, overlooking the important attribute of constraints inherent in CAD shapes, which limits these methods' ability to comprehend CAD shapes fully. To address this issue, we analyzed the effect of constraints, and proposed its deep learning-friendly representation, after that, the Constraint Feature Learning Network (CstNet) was developed to extract and leverage constraints. Our CstNet includes two stages. Stage 1 extracts constraints from B-Rep data or point cloud. Stage 2 leverages coordinates and constraints to enhance the comprehension of CAD shapes. Additionally, we built up the Parametric 20,000 Multi-modal Dataset for the scarcity of labeled B-Rep datasets. Experiments demonstrate that our CstNet achieved state-of-the-art performance on both public and proposed CAD shape datasets. To the best of our knowledge, CstNet is the first constraint-based learning method tailored for CAD shape analysis.

1. Introduction

Parametric point clouds are derived from parametric templates, which consist of primitives, constraints, and dimensional parameters. By specifying all parameters, the templates can be instantiated into CAD shapes, as illustrated in Fig. 1. Parametric point clouds provide detailed information that is essential for various engineering applications, such as model design and product machining.

In recent years, deep learning methods have emerged as powerful tools for point cloud analysis, with models such as PointNet [33], PointNet++ [34], and PointCNN [24] demonstrating significant success across various tasks. These models are primarily designed and evaluated on graphic objects, such as animals, trees, and other free-form shapes, where shape comprehension relies on geometric features visible in contours. However, some CAD shapes, despite exhibiting minimal visual differences, serve distinct purposes due to variations in their functional regions. This similarity in appearance poses challenges in distinguishing them based on geometric features. Notably, variations in the functional regions often introduce differing constraints, as these regions need to fit closely with other parts to perform functions such as transmission and positioning. Thus, distinguishing them from a constraint-based perspective becomes more feasible, as illustrated in Fig. 1.

Additionally, the limited availability of B-Rep datasets poses barriers to deep learning on CAD shapes. Most existing CAD shape datasets consist of mesh files, such as MCB [16] and ESB [12]. While mesh files could approximate the appearance of CAD shapes, lack crucial boundary information. In contrast, B-Rep data [19, 57] serves as the native representation of CAD shapes and is therefore more suitable for dataset construction. However, labeled B-Rep datasets remain relatively scarce, for example, FabWave [1] includes only 2,133 B-Rep files. Although the ABC [18] contains a large number of B-Rep files, it remains unlabeled.

To facilitate the constraint feature learning of CAD shapes, we conducted studies on deep learning methods and dataset development. Traditional constraint definitions are not well-suited for deep learning, as they vary across constraint types and involve multiple possible combinations to represent primitives' relations. To address this challenge, we proposed a novel constraint representation as point-wise

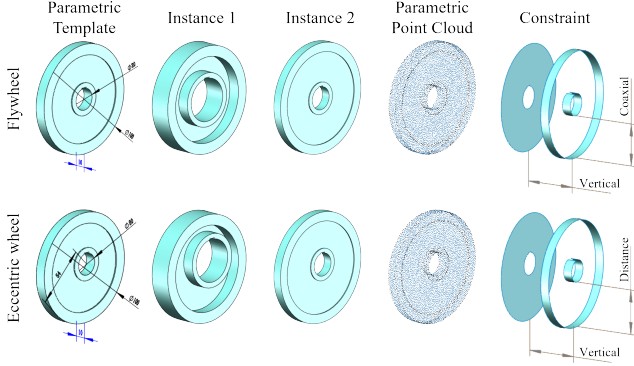


Figure 1. **Motivation.** Some similar CAD shapes serve different functions. The eccentric wheel has a rotation axis that is offset from its outer cylindrical surface, facilitating precise positioning or tension adjustment. In contrast, the flywheel has a coaxial rotation axis with its outer cylindrical surface and is used to store rotational kinetic energy. Although these shapes are challenging to distinguish visually, they can be easily differentiated from the perspective of constraints.

local attributes. Afterward, we developed the CstNet for constraint extraction and feature learning, which consist of two stages. Stage 1 is built for constraint acquisition, if B-Rep data is available, the openCASCADE Technology (OCCT) is used to extract constraints, otherwise, the constraint prediction from point cloud (CST-PCD) module is adopted. The CST-PCD is designed to rely on local features only, enabling it to generalize to unseen datasets after pre-training. Stage 2 leverages both point cloud and constraints for constraint feature learning, which employs both point-level and feature-level attention for effective feature extraction, enhancing the comprehension of CAD shapes. Finally, we built up a multi-modal classification dataset Parametric 20000, which contains B-Rep, Mesh, and point cloud. Given the current scarcity of labeled CAD shape datasets, Parametric 20000 offers researchers an expanded resource for their work. Our contributions are threefold:

- We introduced the deep learning-friendly expression of constraints.
- We designed the CstNet for constraint extraction and constraint feature learning.
- We collected and curated the Parametric 20000 dataset, which consists of mesh, point cloud, and B-Rep data.

Our CstNet has been validated across various tasks, on the mechanical classification dataset MCB [16], our model achieved an overall accuracy improvement of 2.98 % compared to the state-of-the-art, and for mechanical segmentation dataset 360 Gallery [19], that is 6.74 %.

2. Related Work

For the published deep learning methods focusing on CAD shapes are very few, and even fewer aimed at parametric point clouds, this section will provide an overview of existing point cloud learning methods as well as CAD shapes-oriented models. By integrating insights from the above areas, a comprehensive review of the relevant works could be presented.

2.1. Deep learning on point clouds

Point cloud deep learning can be categorized into three types based on data processing approaches: view-based, voxel-based, and point-based methods.

View-based methods typically project the point cloud from multiple views, the obtained figures are then fed in convolutional neural networks (CNNs) for feature extraction [6, 15, 38, 43, 54, 55]. However, these methods face significant challenges when applied to large-scale scanned data, primarily due to the difficulty of covering entire scenes from single-point perspectives, and the choice of projection views significantly impacts recognition performance. Besides that, it cannot be extended to 3D data segmentation or reconstruction easily.

Voxelization-based methods convert point clouds into 3D voxels, and then employ 3D CNNs for feature extraction [17, 20, 30, 36, 41, 48]. However, the size and orientation of the voxels can affect computational efficiency and memory usage. The voxel grid quantization process may lead to geometric detail loss, and the inherent sparsity of point clouds may result in many useless voxels.

Point-based methods directly use points as input, thereby avoiding information loss associated with view-based and voxel-based methods, it is also the most popular point cloud learning method [2, 4, 7, 9, 10, 24, 26–28, 33–35, 39, 42, 47, 49–51, 53, 58–60]. Typically, symmetric functions and k-nearest neighbors (KNN) are employed for feature extraction. However, the unordered nature and transformation invariance of point clouds pose challenges for efficient feature extraction.

2.2. Deep learning on CAD shapes

CAD shapes deep learning can be categorized into three types based on the input data format: B-Rep-based learning, mesh-based learning, and sketch-based learning.

B-Rep-based methods typically involve B-Rep data conversion and feature extraction. Since B-Rep data cannot be directly fed into deep learning models, the challenge lies in converting B-Rep into deep learning compatible format, with graph representation commonly used. These approaches are commonly applied to classification [13], segmentation [5, 19], assembly [14, 44], engineering sketch generation [11], and CAD operation sequence prediction [46, 61].

Mesh-based learning methods use triangle models as input, such as STL and OBJ. Compared to B-Rep, mesh representations lack boundary details, which prevents these methods from leveraging data conversion for improved performance. As a result, contributions often rely on mechanical datasets provided by the authors. These methods are primarily used for classification [29], retrieval [3], segmentation [40], and B-Rep generation [8].

Sketch-based learning takes hand-drawn sketches as input, with outputs typically being engineering sketches [8, 25, 31, 37, 45], 3D models [21, 22, 56], or CAD operation sequences [52]. Most of these models are generative, and frequently utilize transformer modules. A key challenge is incorporating the regularity and connectivity of primitives, which are typically overlooked in graphic object analysis.

While there has been substantial progress in above domains, the engineering applications of parametric point cloud analysis demand further innovation to ensure accuracy and robustness.

3. Method

3.1. Problem Statement

Constraints are crucial for CAD shapes, can they be utilized to enhance deep learning methods' performance? To answer above question, we designed the following validation experiments. The objective is to compare the prisms shown in Fig. 2 with cuboids. In each experiment, only prisms with a specific angle are selected, creating a binary classification task between prisms and cuboids. Consequently, eight independent experiments are conducted to cover all angles. As the prism's angle approaches 90° , its resemblance to cuboids increases, making it progressively more challenging to distinguish them. The constraint-aware model is built on PointNet++ backbone, this model predicts constraints and then adopts it for classification. The constraint representation is defined as the relation between the point attached primitive and a reference plane, more details in supplementary.

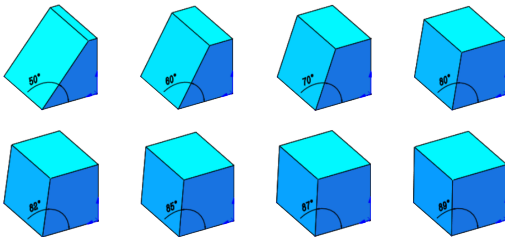


Figure 2. Prisms compared to cuboid.

The experimental results are presented in Fig. 3. For prisms with angle of 50° and 89° , the constraints have little improvement on the results. The reason lies in the 50°

prism differs substantially from the cuboid, while the 89° prism is too similar to the cuboid. For other circumstances, incorporating constraints improves classification accuracy significantly, demonstrating that the constraint enhanced the model's comprehension of CAD shapes.

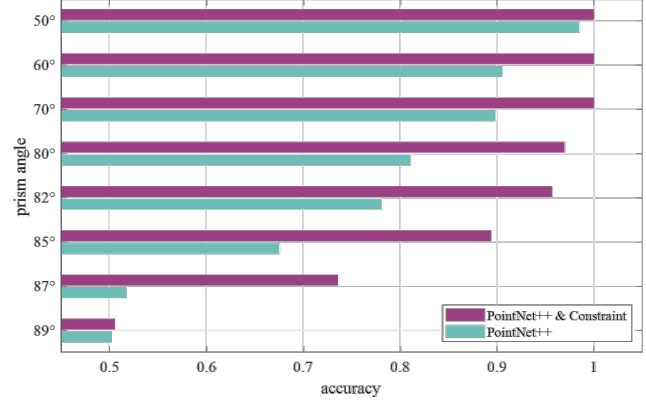


Figure 3. Classification accuracy of validation experiments.

However, the constraint learning method designed in the validation experiments is only applicable to simple scenarios. To develop a more generalized approach, we further investigated the constraint representation and deep learning architecture tailored for parametric point clouds.

3.2. Constraint Representation

Constraint should be defined as point-wise attribute for point cloud, analogous to normal vector, as point cloud is inherently unordered, assigning constraints at the point-wise level ensures that their representation is independent of point permutation.

Following the constraint definitions in CAD software is not applicable. However, once the constraint is applied, the positional relations between primitives become fixed. Therefore, if the type of primitives and their relations are determined, the constraints on CAD shapes can be defined comprehensively.

The point-wise primitive type can be represented as the type of the primitive to which the point is attached, using one-hot encoding.

The positional relation is defined as the combination of main axis direction and adjacency. Considering that the direction of primitives' main axis is unique, as shown in Fig. 4, relations such as parallel and vertical could be derived from the direction of their main axes. However, some dimensional relations can not, such as the cylinders' radius equivalence. Thus, additional data is required to supplement this information.

Since the connected primitives are the basis of CAD shapes, the adjacency and main axis direction impose limitations on the distance and size of primitives. For example,

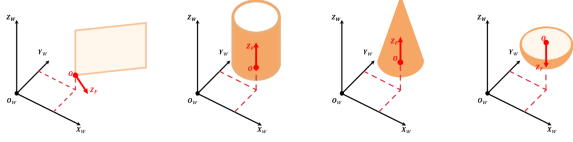


Figure 4. **Main axis of primitives.** Plane: normal vector. Cylinder, cone, and sphere: rotation axis.

in a cuboid, the adjacency and normal of the six faces ensure that the distance between the top and bottom faces equals the height of the front face, and the size of the back face is the same as the front one. Therefore, if the adjacency is combined with main axis directions, the positional relation can be determined comprehensively.

Adjacency represents the connection between primitives and cannot be expressed as point-wise attribute directly. The edges are key indicators of adjacency, with each edge corresponding to two adjacent primitives, adjacency can therefore be inferred from edges. For point cloud, an edge can be represented by marking points near it, thus, point-wise adjacency is expressed as whether the point is near an edge, which can be represented by two-channel one-hot vector.

In summary, each composition of constraints in parametric point cloud is illustrated in Fig. 5, and each point with constraint is expressed as (Coordinate, Primitive Type, Main Axis Direction, Adjacency).

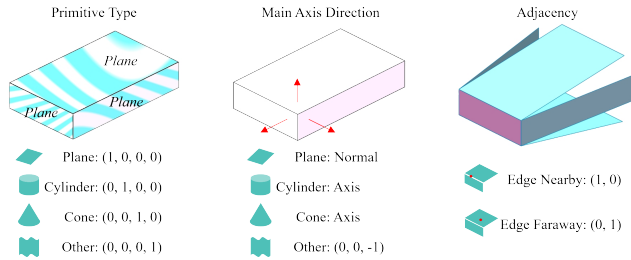


Figure 5. **Constraint representation of parametric point cloud.**

3.3. Method Overview

Our CstNet and module details are depicted in the top and bottom sides of Fig. 6 respectively. It should be noted that the CST-PCD module requires pre-training, and once the pre-training is completed, its parameters are kept frozen. Given the locality of the constraints expression we designed, the pre-trained CST-PCD module is able to generalize to other unseen CAD shape datasets directly. In this work, the dataset for pre-training CST-PCD module comes from ABC [18].

3.4. Constraint Acquisition

When B-Rep data is available, the CST-BRep module can be used to compute constraints.

For the input B-Rep data, tessellation is performed by OCCT to generate a mesh model, followed by Poisson disk sampling [23] via pymeshlab to ensure a uniform point distribution and control the point count, if point cloud generation is not needed, this step could be skipped.

For adjacency computation, we identify valid edges first. In this study, an edge is considered invalid if the two adjacent primitives are smoothly connected along the edge, this work is accomplished by OCCT. Next, we compute the distance from each point to all valid edges. A point is marked as near an edge if the minimum distance is below a threshold (determined by the model surface area, set to $0.08 \times Area/4\pi$ in this paper). For the primitive type and main axis direction of a point, we first determine which primitive it attached, OCCT is then used to analyze the primitive, providing both the primitive type and main axis direction.

In the absence of B-Rep data, such as working with mesh or voxel models, it can be converted into point cloud, after which the CST-PCD module can be used to predict constraints. Since each point's constraints are local information, the computation only requires data from its neighboring points, meaning that global information is unnecessary. The constraint computation of a point p could be divided into the following steps:

Step 1. Identify neighbor points around p .

Step 2. From all neighbor points, identify which belongs to the same primitive as p , these points are referred to as valid points.

Step 3. Fit shapes such as cylinders or planes using valid points, and determine the primitive type with the smallest fitting error.

Step 4. Based on the valid points and the primitive type, calculate the main axis direction and assess whether the point is near an edge.

While the above process can be carried out using traditional methods, it is highly complex, which is why a deep learning model is employed to achieve the same.

The design of CST-PCD module is inspired by the aforementioned calculation process. For **Step 1**, which involves finding neighbor points, the traditional approach is to use the K Nearest Neighbors (KNN) algorithm, which identifies neighbors within a sphere. However, for constraint computation, it is more effective to search for neighbors along the shape's surface. This approach captures more relevant points while reducing the influence of redundant points, as shown in Fig. 7. To this end, we proposed a neighbor searching method called SurfaceKNN, details in supplementary.

For **Step 2**, which involves identifying valid points from

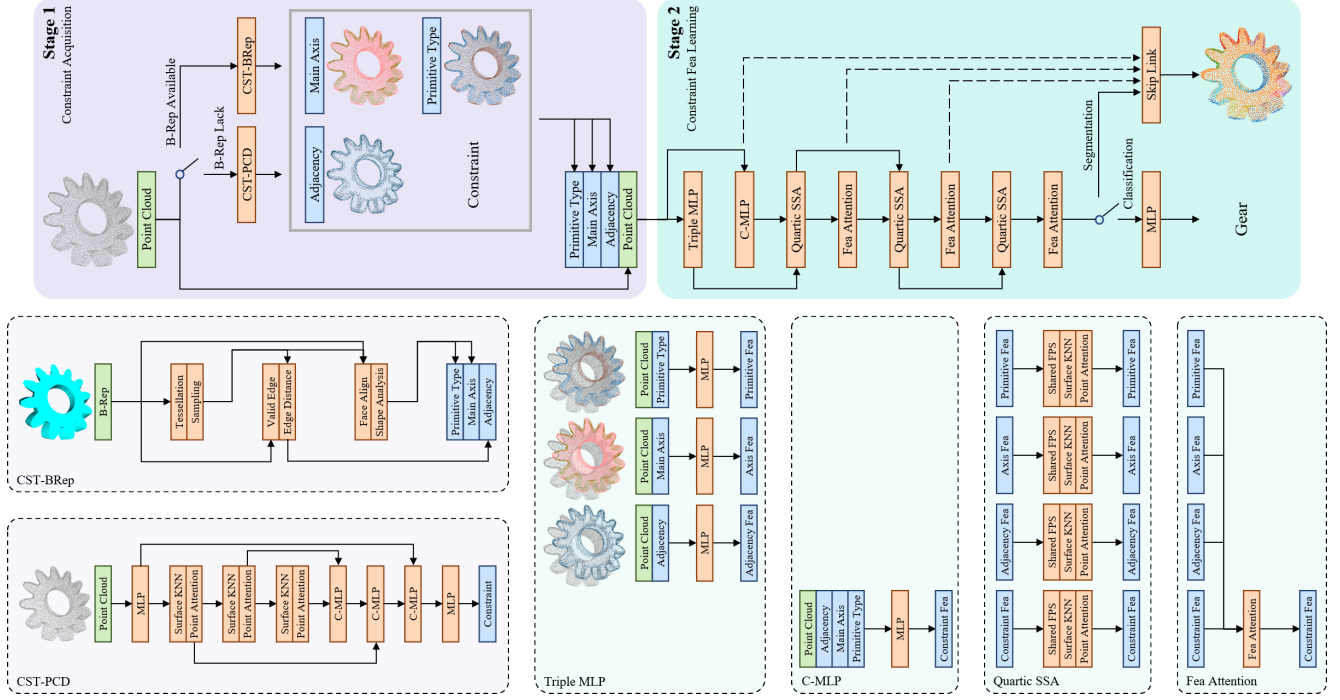


Figure 6. **Overview of CstNet.** The top side illustrates the overall architecture of CstNet, comprising two stages. Stage 1 is designed for constraint acquisition. When B-Rep data is available, the CST-BRep module is utilized to extract constraints; otherwise, use the CST-PCD module. Stage 2 performs constraint feature learning, facilitating a deeper understanding of CAD shapes. The bottom side presents the details of module design.

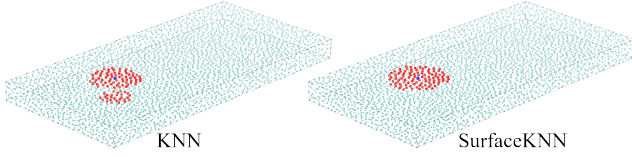


Figure 7. **Comparison of KNN and SurfaceKNN.** Blue point: center, red point: neighbor.

neighbors, the attention mechanism between points is employed to approximate this process, which applies different weights to neighbor points when updating the center point’s embedding. We designed the point attention layer based on vector self-attention, the relation between points is designed as embedding subtraction, as shown in Eq. (1).

$$\mathbf{f}'_i = \sum_{\mathbf{f}_j \in \mathcal{N}_i} \rho \left(mlp(Q(\mathbf{f}_i) - K(\mathbf{f}_j)) \right) \odot V(\mathbf{f}_i). \quad (1)$$

Where \mathcal{N}_i is the feature collection of all neighbor points around \mathbf{p}_i , ρ is the normalization function (softmax in this paper), and \odot denotes element-wise multiplication. $Q(\mathbf{f})$, $K(\mathbf{f})$, and $V(\mathbf{f})$ are defined in the same way by concatenating \mathbf{f} with the positional encoding Δ and then feeding it into MLP, where Δ is defined as $\Delta = \mathbf{p}_i - \mathbf{p}_j$.

Step 3 and **Step 4** involve determining the Primitive Type and Main Axis Direction, both steps can be accomplished by MLPs. We employed a U-Net-like structure to enhance information utilization. In the CST-PCD module, C-MLP refers to concatenating the input tensors and feeding them into MLPs. The final MLP in this module consists of three parallel MLPs with the same input, where the outputs correspond to Primitive Type, Main Axis Direction, and Adjacency.

The structure of CST-PCD module reveals that only local information is utilized, which aligns with the inherently local nature of the constraint representation we designed. For no global information is incorporated and most CAD shapes consist of a limited set of local geometry, such as plane, cylinder, and sphere, the CST-PCD can generalize to unseen datasets if pre-trained on a large dataset. As a result, our CST-PCD enables the effective use of existing unlabeled B-Rep datasets, making it possible to serve meaningful tasks.

3.5. Constraint Feature Learning

Stage 2 of CstNet is designed to leverage constraints to deepen the model’s understanding of CAD shapes. The designed architecture extracts features from Primitive Type, Main Axis Direction, and Adjacency separately, attention

between features is then applied to update constraint feature. The structure and module details are illustrated in Fig. 6.

The Triple MLP takes the point cloud, Primitive Type, Main Axis Direction, and Adjacency as inputs. In this module, the point cloud is concatenated with the Primitive Type, Main Axis Direction, and Adjacency separately before being fed into three individual MLPs. The outputs are the Primitive Feature, Axis Feature, and Adjacency Feature, respectively.

In the C-MLP layer, point cloud is concatenated with Primitive Type, Main Axis Direction, Adjacency, and then feeds into MLP, with the output being the Parametric Feature.

The Quartic SSA layer takes the Primitive Feature, Axis Feature, Adjacency Feature, and Parametric Feature as input. This layer consists of four paths, each processing the corresponding feature independently. In each path, Farthest Point Sampling (FPS) is performed to reduce the point scale. Subsequently, SurfaceKNN is used to search for neighbors of each sampled point. The output of FPS and SurfaceKNN are shared across the four paths. Finally, point attention is employed for updating sampled points' feature by its neighbors, with a slight modification in the positional encoding Δ of Eq. (1). For the path takes XYZ & Main Axis Direction as input, $\Delta = [(p_i - p_j) \parallel (n_i - n_j)]$, n_i represents the main axis direction of p_i . For the paths that use XYZ & Primitive Type or Adjacency as input, $\Delta = [(p_i - p_j) \parallel a_i \parallel a_j]$, where a_i, a_j is the one-hot encoding of Primitive Type or Adjacency, $[\cdot \parallel \cdot]$ indicates concatenation in feature channel. Through sampling, neighbor searching, and attention, the point cloud is down-scaled and features are updated.

The Fea Attention layer also takes the Primitive Feature, Axis Feature, Adjacency Feature, and Parametric Feature as input, attention between features is employed to update the constraint feature efficiently. This design considers that different points may focus on different features, for example, points near edge may focus more on the Adjacency Feature, while others may pay more attention to the Primitive or Axis Feature. The Fea Attention is developed by vector attention as formulated in Eq. (2).

$$f'_{cst} = \sum_{f_j \in \mathcal{F}} \rho \left(mlp(Q(f_{cst}) - K(f_j)) \right) \odot V(f_{cst}). \quad (2)$$

In which $\mathcal{F} = \{f_{pmt}, f_{axs}, f_{adj}, f_{cst}\}$, f_{pmt} is Primitive Feature, f_{axs} is Axis Feature, f_{adj} is Adjacency Feature, and f_{cst} is Constraint Feature. Δ is defined as one-hot encoding of f_j type.

For downstream tasks, if classification is required, the final constraint feature can be fed into MLP and softmax. For

segmentation tasks, upsampling and skip link concatenation similar to those in PointNet++ [34] can be applied.

4. Experiments

4.1. Experimental Settings

In general, we train CstNet using the Negative Log Likelihood Loss (NLLoss) and optimized by Adam optimization for 200 epochs, with a weight decay of 0.0001 and an initial learning rate of 0.0001. We use StepLR learning rate scheduler, with step size of 20 and gamma of 0.7. The batch size is 16. All experiments are performed on GeForce RTX 4090 GPU.

Parametric 20000 dataset: our Parametric 20000 dataset contains 19,739 multi-modal instances categorized into 75 classes. Each instance includes B-Rep data, mesh, and point cloud. All B-Rep data are collected from the following three sources. More details in the supplementary.

Sources 1 (36.05 %): Downloaded and purified from TraceParts [16]. The CAD shapes on TraceParts are collected from manufacturing companies.

Sources 2 (24.12 %): Provided by a CAD company¹ that collaborates with our team. These shapes are all mechanical components.

Sources 3 (39.83 %): Instantiated from parametric templates designed by our team. These templates are designed based on common mechanical structures.

Our Parametric 20000 dataset encompasses various common formats of CAD shapes, making it suitable for a wide range of tasks. The careful selection and purification process undertaken by our team further ensures its high quality.

4.2. Constraint Acquisition

The extraction of constraints from B-Rep data is accomplished by CST-BRep module, with results visualized in the "GT" column of Fig. 8. By referring to the model row, this module performs well in extracting three components of constraint.

Extracting constraints from point cloud is achieved by CST-PCD module. The training set is sourced from 25 trunks of ABC [18], with each trunk containing 10,000 B-Rep files. We utilized CST-BRep module to extract constraints as Ground Truth for model training. After the training finished, the prediction accuracy of Primitive Type reached 94.23 %, for Adjacency, that is 94.62 %, and the MSE loss for Main Axis Direction is 0.0559.

In subsequent classification and segmentation tasks, the above pre-trained CST-PCD module is utilized to predict constraints with its weights frozen and no further updates. To ensure that only point cloud is used as input across all methods in comparison, even when B-Rep data is available,

¹<https://www.newdimchina.com/>

the CST-BRep module will not be activated to obtain constraints.

After CST-PCD module was pre-trained, we evaluated it on a new trunk of ABC. The visualization of constraint prediction is shown in the "Pred." column of Fig. 8. After traversing this trunk, the prediction accuracy of Primitive Type reached 91.19 %, for Adjacency, that is 90.24 %, the MSE loss of Main Axis Direction is 0.0998, above demonstrating the strong capability for constraint prediction.

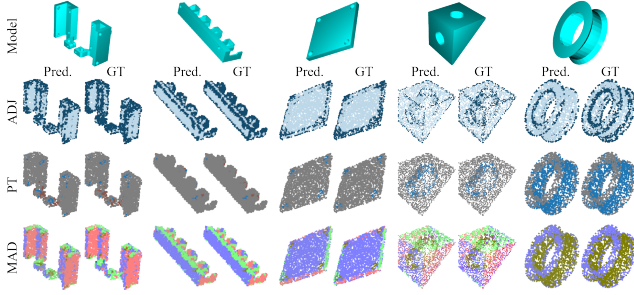


Figure 8. **Constraint prediction on ABC.** MAD: Main Axis Direction. PT: Primitive Type. ADJ: Adjacency (whether point is near edge). Main Axis Direction has been processed for visualization, details in supplementary.

Additionally, we evaluated the pre-trained CST-PCD module on the CAD shape dataset MCB [16] to predict constraints. For the MCB consists of mesh files, it was not possible to extract Ground Truth constraints for comparison. Based on the results visualized in Fig. 9, CST-PCD demonstrated a high level of constraint prediction accuracy even on an unseen dataset.

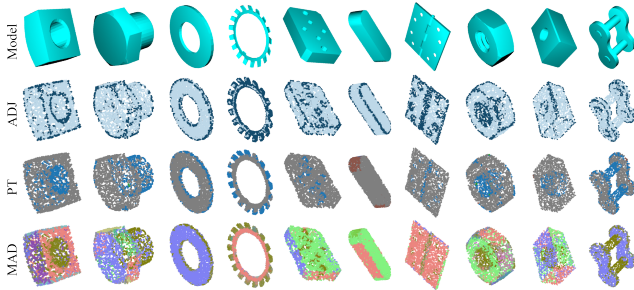


Figure 9. **Constraint prediction on MCB.**

4.3. Classification

The classification results on the Parametric 20000 dataset are presented in Tab. 1, where our CstNet outperformed other methods across both metrics. Additionally, the instance accuracy of all methods is below 90 %, with a notable performance gap between them, indicating that this dataset poses challenges and effectively differentiates between methods.

Table 1. **Classification results on Parametric 20000.** Acc: accuracy over instance %, Acc*: accuracy over class %, F1: F1-score, mAP: mean average precision %.

Method	Acc	Acc*	F1	mAP
PointCNN [24]	61.92	55.29	53.97	40.99
PointNet [33]	75.61	74.08	74.23	82.15
PointNet++ [34]	82.89	86.80	82.31	88.05
PointConv [47]	80.53	82.10	81.86	86.54
DGCNN [42]	85.99	88.20	87.20	89.20
3DGCN [26]	86.19	86.31	85.37	87.64
Ours	89.93	91.04	90.32	92.32

We conducted evaluations on the CAD shape dataset MCB [16], with results presented in Tab. 2. Our CstNet achieved the highest scores across all metrics on MCB-A, but performed less effectively on MCB-B. This discrepancy may stem from the composition of MCB: MCB-A includes shapes from TraceParts (69.27 %), 3D Warehouse (21.70 %), and GrabCAD (9.03 %), while MCB-B is limited to shapes from 3D Warehouse and GrabCAD. TraceParts provides data from manufacturing companies, whereas 3D Warehouse and GrabCAD contain shapes for general usage [16]. As the CST-PCD module in CstNet is pre-trained on ABC, which primarily comprises mechanical components, this pre-training may lead to poor constraint prediction performance on MCB-B, thereby influencing the classification results.

4.4. Segmentation

We conducted experiments on the mechanical segmentation dataset 360 Gallery [19], which contains point clouds with segmentation labels based on CAD modeling operations. However, this labeling approach presents disadvantages for point cloud segmentation. For example, a cube in this dataset has four faces labeled as "ExtrudeSide" and two faces labeled as "ExtrudeEnd", which poses an unrealistic task for point cloud networks. Additionally, the distribution of points across different labels is highly imbalanced. For instance, points labeled as "ExtrudeSide" account for 45.94 %, while those labeled as "RevolveEnd" make up only 0.12 %. Despite these limitations, to our knowledge, 360 Gallery is currently the only publicly available point cloud dataset for CAD shape segmentation tasks.

The segmentation results are presented in Tab. 3, where our method outperforms the state-of-the-art methods on most metrics. The results also highlight the limitations of 360 Gallery in terms of point cloud segmentation. Apart from "ExtrudeSide" and "ExtrudeEnd", none of the models were able to differentiate the other segmentation categories except DGCNN managed to predict "RevolveSide" with a low mIoU.

Table 2. **Classification results on MCB.** A / B column: results of MCB A / B subset.

Method	Acc.instance %		Acc.class %		F1-score		mAP %	
	A	B	A	B	A	B	A	B
PointCNN [24]	93.89	93.67	81.85	86.80	83.86	88.63	90.13	93.86
PointNet [33]	86.78	80.36	67.70	65.30	86.55	79.89	74.08	71.66
PointNet++ [34]	87.45	93.91	73.68	87.97	88.32	73.45	91.33	91.37
SpiderCNN [53]	93.59	89.31	79.70	79.29	81.30	80.72	86.64	82.47
PointConv [47]	93.25	90.64	80.24	80.17	71.31	76.07	82.19	86.09
DGCNN [42]	92.54	90.75	74.47	78.17	76.12	79.69	74.27	79.73
3DGCN [26]	93.71	92.13	78.71	84.31	84.59	79.24	84.35	84.35
Ours	96.87	92.61	89.21	85.94	89.85	85.68	93.17	91.25

Table 3. **Part Segmentation Results on 360 Gallery.** PN: PointNet. PN2: PointNet++. DGN: DGCNN. 3DN: 3DGCN. OA: overall accuracy %. mIoU: instance mIoU %. mIoU*: class mIoU %. ESide: Extrude Side mIoU %, EEnd: Extrude End mIoU %. Other segmentation categories' mIoU are all 0 except RevolveSide mIoU of DGCNN is 9.60 %, more details in supplementary.

Method	OA	mIoU	mIoU*	ESide	EEnd
PN [33]	42.13	18.89	7.04	19.83	36.47
PN2 [34]	58.18	26.98	11.27	49.80	40.36
DGN [42]	64.02	35.54	14.36	54.48	50.82
3DN [26]	60.58	33.03	12.23	50.67	47.20
Ours	70.76	46.65	20.51	61.29	60.65

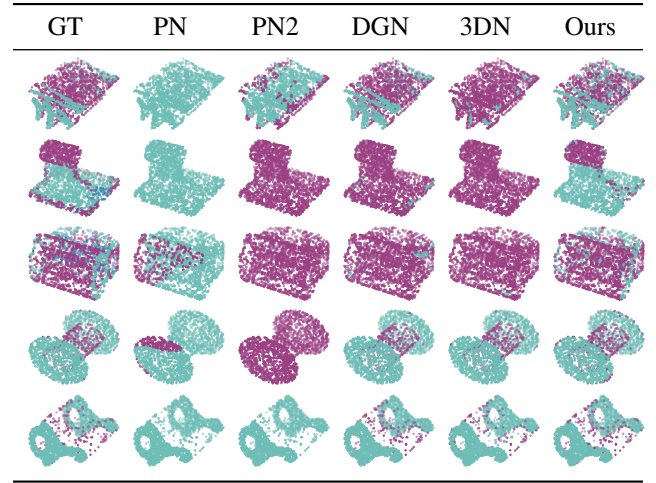
A portion of the segmentation results on 360 Gallery test set are shown in Tab. 4, where our CstNet shows segmentation results closest to the Ground Truth. PointNet's segmentation differs from other methods, for instance, in the third and fourth rows, PointNet mistakenly segments a single primitive into two different categories. This discrepancy likely arises from the model's inability to effectively capture local features.

4.5. Ablation Studies

Our model leverages all three components of constraint: Primitive Type, Main Axis Direction, and Adjacency. Additionally, we utilized the SurfaceKNN to obtain more suitable neighbors for each point. To validate the effectiveness of our design, we conducted a series of experiments on Parametric 20000 dataset.

For each component of constraint, we evaluated their importance by disabling one at a time. This operation is performed by setting it as a zero tensor before feeding into the model. The results are presented in Tab. 5, which show that all three components contribute to improving the performance of our CstNet.

To assess the effectiveness of SurfaceKNN, we com-

Table 4. **Visualization of part segmentation on 360 Gallery.** GT: ground truth. PN: PointNet [33]. PN2: PointNet++ [34]. DGN: DGCNN [42]. 3DN: 3DGCN [26].

pared it with KNN. From Tab. 5, it can be concluded that in most cases, our SurfaceKNN outperforms KNN. However, when the Primitive Type is disabled, the results are similar between the two methods, indicating that SurfaceKNN primarily enhances the effectiveness of the Primitive Feature.

5. Conclusions

In this paper, we studied the CAD shapes and introduced the constraints expression which is suitable for deep learning methods. Afterward, we proposed the CstNet for extracting and learning constraint features. Additionally, we built up a multimodal CAD shape classification dataset Parametric 20000. Experimental results on both the public datasets and proposed dataset demonstrate that our CstNet achieves state-of-the-art performance across multiple metrics. Comprehensive ablation studies further validate that each component of constraint and SurfaceKNN contributes

Table 5. **Effects on Parametric 20000 dataset with varying neighbor search and constraints.** Row 3 - 6: SurfaceKNN, Row 7 - 10: KNN.

Constraint			Acc	Acc*	F1	mAP
MAD	ADJ	PT				
✓	✓	✓	89.93	91.04	90.32	92.32
✗	✓	✓	86.32	89.05	88.38	90.59
✓	✗	✓	88.14	89.61	88.64	91.35
✓	✓	✗	88.68	88.94	89.01	91.22
✓	✓	✓	89.03	90.00	89.22	91.43
✗	✓	✓	85.04	85.93	85.74	88.08
✓	✗	✓	87.27	88.23	87.98	90.00
✓	✓	✗	88.73	88.97	88.91	91.21

to improve the performance of CstNet.

CAD shapes possess numerous attributes. In this paper, we analyze the constraints from a functional perspective. In future work, we plan to investigate additional aspects such as part design and manufacturing processes, to achieve a deeper understanding of CAD shapes.

References

- [1] A. Angrish, B. Craver, and B. Starly. Fabsearch: A 3d cad model-based search engine for sourcing manufacturing services. *Journal of Computing and Information Science in Engineering*, 19(4), 2019. Export Date: 08 October 2024; Cited By: 23. [1](#)
- [2] M. Atzmon, H. Maron, and Y. Lipman. Point convolutional neural networks by extension operators. *ACM Transactions on Graphics*, 37(4), 2018. Export Date: 31 July 2024; Cited By: 222. [2](#)
- [3] D. Y. Chen, X. P. Tian, Y. T. Shen, and M. Ouhyoung. On visual similarity based 3d model retrieval. In *Computer Graphics Forum*, volume 22, pages 223–232, 2003. Export Date: 28 June 2024; Cited By: 1323. [3](#)
- [4] Yan Chen, Di Huang, Zhichao Liao, Xi Cheng, Xinghui Li, and Lone Zeng. Training-free point cloud recognition based on geometric and semantic information fusion. *arXiv preprint arXiv:2409.04760*, 2024. [2](#)
- [5] E. Dupont, K. Cherenkova, A. Kacem, S. A. Ali, I. Arzhanikov, G. Gusev, and D. Aouada. Cadops-net: Jointly learning cad operation types and steps from boundary-representations. In *Proceedings - 2022 International Conference on 3D Vision, 3DV 2022*, pages 114–123, 2022. Export Date: 06 July 2024; Cited By: 2. [2](#)
- [6] Y. Feng, Z. Zhang, X. Zhao, R. Ji, and Y. Gao. Gvcnn: Group-view convolutional neural networks for 3d shape recognition. In *Proceedings of the IEEE Computer Society Conference on Computer Vision and Pattern Recognition*, pages 264–272, 2018. Export Date: 31 July 2024; Cited By: 502. [2](#)
- [7] A. Goyal, H. Law, B. Liu, A. Newell, and J. Deng. Revisiting point cloud shape classification with a simple and effective baseline. In *Proceedings of Machine Learning Research*, volume 139, pages 3809–3820, 2021. Export Date: 31 July 2024; Cited By: 92. [2](#)
- [8] H. Guo, S. Liu, H. Pan, Y. Liu, X. Tong, and B. Guo. Complexgen: Cad reconstruction by b-rep chain complex generation. *ACM Transactions on Graphics*, 41(4), 2022. Export Date: 23 July 2024; Cited By: 20. [3](#)
- [9] M. H. Guo, J. X. Cai, Z. N. Liu, T. J. Mu, R. R. Martin, and S. M. Hu. Pct: Point cloud transformer. *Computational Visual Media*, 7(2):187–199, 2021. Export Date: 31 July 2024; Cited By: 917. [2](#)
- [10] Q. Huang, W. Wang, and U. Neumann. Recurrent slice networks for 3d segmentation of point clouds. In *Proceedings of the IEEE Computer Society Conference on Computer Vision and Pattern Recognition*, pages 2626–2635, 2018. Export Date: 31 July 2024; Cited By: 391. [2](#)
- [11] F. Hähnlein, C. Li, N. J. Mitra, and A. Bousseau. Cad2sketch. *ACM Transactions on Graphics*, 41(6), 2022. Export Date: 23 July 2024; Cited By: 1. [2](#)
- [12] S. Jayanti, Y. Kalyanaraman, N. Iyer, and K. Ramani. Developing an engineering shape benchmark for cad models. *CAD Computer Aided Design*, 38(9):939–953, 2006. Export Date: 08 October 2024; Cited By: 280. [1](#)
- [13] P. K. Jayaraman, A. Sanghi, J. G. Lambourne, K. D. D. Willis, T. Davies, H. Shayani, and N. Morris. Uv-net: Learning from boundary representations. In *Proceedings of the IEEE Computer Society Conference on Computer Vision and Pattern Recognition*, pages 11698–11707, 2021. Export Date: 28 June 2024; Cited By: 27. [2](#)
- [14] Benjamin Jones, Dalton Hildreth, Duowen Chen, Ilya Baran, Vladimir G. Kim, and Adriana Schulz. Automate: a dataset and learning approach for automatic mating of cad assemblies. *ACM Transactions on Graphics*, 40(6):1–18, Dec. 2021. [2](#)
- [15] E. Kalogerakis, M. Averkiou, S. Maji, and S. Chaudhuri. 3d shape segmentation with projective convolutional networks. In *Proceedings - 30th IEEE Conference on Computer Vision and Pattern Recognition, CVPR 2017*, volume 2017-January, pages 6630–6639, 2017. Export Date: 31 July 2024; Cited By: 256. [2](#)
- [16] S. Kim, H. G. Chi, X. Hu, Q. Huang, and K. Ramani. A large-scale annotated mechanical components benchmark for classification and retrieval tasks with deep neural networks. In *Lecture Notes in Computer Science (including subseries Lecture Notes in Artificial Intelligence and Lecture Notes in Bioinformatics)*, volume 12363 LNCS, pages 175–191, 2020. Export Date: 07 October 2024; Cited By: 33. [1](#), [2](#), [6](#), [7](#)
- [17] R. Klokov and V. Lempitsky. Escape from cells: Deep kd-networks for the recognition of 3d point cloud models. In *Proceedings of the IEEE International Conference on Computer Vision*, volume 2017-October, pages 863–872, 2017. Export Date: 31 July 2024; Cited By: 857. [2](#)
- [18] S. Koch, A. Matveev, Z. Jiang, F. Williams, A. Artemov, E. Burnaev, M. Alexa, D. Zorin, and D. Panozzo. Abc: A big cad model dataset for geometric deep learning. In *Proceedings of the IEEE Computer Society Conference on Computer Vision and Pattern Recognition*, volume 2019-June, pages 9593–9603, 2019. Export Date: 08 October 2024; Cited By:

279. 1, 4, 6
- [19] J. G. Lambourne, K. D. D. Willis, P. K. Jayaraman, A. Sanghi, P. Meltzer, and H. Shayani. Brepnet: A topological message passing system for solid models. In *Proceedings of the IEEE Computer Society Conference on Computer Vision and Pattern Recognition*, pages 12768–12777, 2021. Export Date: 28 June 2024; Cited By: 31. 1, 2, 7
 - [20] T. Le and Y. Duan. Pointgrid: A deep network for 3d shape understanding. In *Proceedings of the IEEE Computer Society Conference on Computer Vision and Pattern Recognition*, pages 9204–9214, 2018. Export Date: 31 July 2024; Cited By: 324. 2
 - [21] C. Li, H. Pan, A. Bousseau, and N. J. Mitra. Sketch2cad: Sequential cad modeling by sketching in context. *ACM Transactions on Graphics*, 39(6), 2020. Export Date: 23 July 2024; Cited By: 42. 3
 - [22] C. Li, H. Pan, A. Bousseau, and N. J. Mitra. Free2cad: Parsing freehand drawings into cad commands. *ACM Transactions on Graphics*, 41(4), 2022. Export Date: 23 July 2024; Cited By: 27. 3
 - [23] Hongwei Li. *Poisson disk sampling: modern techniques*. Thesis, The Hong Kong University of Science and Technology Library, 2010. 4
 - [24] Y. Li, R. Bu, M. Sun, W. Wu, X. Di, and B. Chen. Pointcnn: Convolution on x-transformed points. In *Advances in Neural Information Processing Systems*, volume 2018-December, pages 820–830, 2018. Export Date: 08 October 2024; Cited By: 1859. 1, 2, 7, 8
 - [25] Zhichao Liao, Di Huang, Heming Fang, Yue Ma, Fengyuan Piao, Xinghui Li, Long Zeng, and Pingfa Feng. Free-hand sketch generation from mechanical components. *arXiv preprint arXiv:2408.05966*, 2024. 3
 - [26] Z. H. Lin, S. Y. Huang, and Y. C. F. Wang. Learning of 3d graph convolution networks for point cloud analysis. *IEEE Transactions on Pattern Analysis and Machine Intelligence*, 44(8):4212–4224, 2022. Export Date: 08 October 2024; Cited By: 35. 2, 7, 8, 5
 - [27] Y. Liu, B. Fan, S. Xiang, and C. Pan. Relation-shape convolutional neural network for point cloud analysis. In *Proceedings of the IEEE Computer Society Conference on Computer Vision and Pattern Recognition*, volume 2019-June, pages 8887–8896, 2019. Export Date: 31 July 2024; Cited By: 664.
 - [28] X. Ma, C. Qin, H. You, H. Ran, and Y. Fu. Rethinking network design and local geometry in point cloud: A simple residual mlp framework. In *ICLR 2022 - 10th International Conference on Learning Representations*, 2022. Export Date: 31 July 2024; Cited By: 172. 2
 - [29] B. Manda, P. Bhaskare, and R. Muthuganapathy. A convolutional neural network approach to the classification of engineering models. *IEEE Access*, 9:22711–22723, 2021. Export Date: 28 June 2024; Cited By: 18. 3
 - [30] D. Maturana and S. Scherer. Voxnet: A 3d convolutional neural network for real-time object recognition. In *IEEE International Conference on Intelligent Robots and Systems*, volume 2015-December, pages 922–928, 2015. Export Date: 31 July 2024; Cited By: 2809. 2
 - [31] W. R. Para, S. F. Bhat, P. Guerrero, T. Kelly, N. Mitra, L. Guibas, and P. Wonka. Sketchgen: Generating constrained cad sketches. In *Advances in Neural Information Processing Systems*, volume 7, pages 5077–5088, 2021. Export Date: 07 July 2024; Cited By: 23. 3
 - [32] Janusz Pobożniak. Algorithm for iso 14649 (step-nc) feature recognition. *Management and Production Engineering Review*, 4(4):50–58, Dec. 2013. 1
 - [33] C. R. Qi, H. Su, K. Mo, and L. J. Guibas. Pointnet: Deep learning on point sets for 3d classification and segmentation. In *Proceedings - 30th IEEE Conference on Computer Vision and Pattern Recognition, CVPR 2017*, volume 2017-January, pages 77–85, 2017. Export Date: 31 July 2024; Cited By: 9040. 1, 2, 7, 8, 5
 - [34] C. R. Qi, L. Yi, H. Su, and L. J. Guibas. Pointnet++: Deep hierarchical feature learning on point sets in a metric space. In *Advances in Neural Information Processing Systems*, volume 2017-December, pages 5100–5109, 2017. Export Date: 31 July 2024; Cited By: 6263. 1, 6, 7, 8, 2, 5
 - [35] S. Qiu, S. Anwar, and N. Barnes. Geometric back-projection network for point cloud classification. *IEEE Transactions on Multimedia*, 24:1943–1955, 2022. Export Date: 31 July 2024; Cited By: 110. 2
 - [36] G. Riegler, A. O. Ulusoy, and A. Geiger. Octnet: Learning deep 3d representations at high resolutions. In *Proceedings - 30th IEEE Conference on Computer Vision and Pattern Recognition, CVPR 2017*, volume 2017-January, pages 6620–6629, 2017. Export Date: 31 July 2024; Cited By: 1052. 2
 - [37] A. Seff, W. Zhou, N. Richardson, and R. P. Adams. Vitruvion: A generative model of parametric cad sketches. In *ICLR 2022 - 10th International Conference on Learning Representations*, 2022. Export Date: 07 July 2024; Cited By: 9. 3
 - [38] H. Su, S. Maji, E. Kalogerakis, and E. Learned-Miller. Multi-view convolutional neural networks for 3d shape recognition. In *Proceedings of the IEEE International Conference on Computer Vision*, volume 2015 International Conference on Computer Vision, ICCV 2015, pages 945–953, 2015. Export Date: 31 July 2024; Cited By: 2865. 2
 - [39] H. Thomas, C. R. Qi, J. E. Deschaud, B. Marcotegui, F. Goulette, and L. Guibas. Kpconv: Flexible and deformable convolution for point clouds. In *Proceedings of the IEEE International Conference on Computer Vision*, volume 2019-October, pages 6410–6419, 2019. Export Date: 31 July 2024; Cited By: 1705. 2
 - [40] M. A. Uy, Y. Y. Chang, M. Sung, P. Goel, J. Lambourne, T. Birdal, and L. Guibas. Point2cyl: Reverse engineering 3d objects from point clouds to extrusion cylinders. In *Proceedings of the IEEE Computer Society Conference on Computer Vision and Pattern Recognition*, volume 2022-June, pages 11840–11850, 2022. Export Date: 23 July 2024; Cited By: 17. 3
 - [41] P. S. Wang, Y. Liu, Y. X. Guo, C. Y. Sun, and X. Tong. O-cnn: Octree-based convolutional neural networks for 3d shape analysis. In *ACM Transactions on Graphics*, volume 36, 2017. Export Date: 31 July 2024; Cited By: 851. 2
 - [42] Y. Wang, Y. Sun, Z. Liu, S. E. Sarma, M. M. Bronstein, and J. M. Solomon. Dynamic graph cnn for learning on point clouds. *ACM Transactions on Graphics*, 38(5), 2019. Export

Date: 08 October 2024; Cited By: 3926. [2](#), [7](#), [8](#), [5](#)

- [43] X. Wei, R. Yu, and J. Sun. View-gcn: View-based graph convolutional network for 3d shape analysis. In *Proceedings of the IEEE Computer Society Conference on Computer Vision and Pattern Recognition*, pages 1847–1856, 2020. Export Date: 31 July 2024; Cited By: 197. [2](#)
- [44] Karl D.D. Willis, Pradeep Kumar Jayaraman, Hang Chu, Yunsheng Tian, Yifei Li, Daniele Grandi, Aditya Sanghi, Linh Tran, Joseph G. Lambourne, Armando Solar-Lezama, and Wojciech Matusik. Joinable: Learning bottom-up assembly of parametric cad joints. In *2022 IEEE/CVF Conference on Computer Vision and Pattern Recognition (CVPR)*. IEEE, June 2022. [2](#)
- [45] K. D. D. Willis, P. K. Jayaraman, J. G. Lambourne, H. Chu, and Y. Pu. Engineering sketch generation for computer-aided design. In *IEEE Computer Society Conference on Computer Vision and Pattern Recognition Workshops*, pages 2105–2114, 2021. Export Date: 07 July 2024; Cited By: 30. [3](#)
- [46] R. Wu, C. Xiao, and C. Zheng. Deepcad: A deep generative network for computer-aided design models. In *Proceedings of the IEEE International Conference on Computer Vision*, pages 6752–6762, 2021. Export Date: 23 July 2024; Cited By: 47. [2](#)
- [47] W. Wu, Z. Qi, and L. Fuxin. Pointconv: Deep convolutional networks on 3d point clouds. In *Proceedings of the IEEE Computer Society Conference on Computer Vision and Pattern Recognition*, volume 2019-June, pages 9613–9622, 2019. Export Date: 09 October 2024; Cited By: 1264. [2](#), [7](#), [8](#)
- [48] Z. Wu, S. Song, A. Khosla, F. Yu, L. Zhang, X. Tang, and J. Xiao. 3d shapenets: A deep representation for volumetric shapes. In *Proceedings of the IEEE Computer Society Conference on Computer Vision and Pattern Recognition*, volume 07-12-June-2015, pages 1912–1920, 2015. Export Date: 31 July 2024; Cited By: 4378. [2](#)
- [49] T. Xiang, C. Zhang, Y. Song, J. Yu, and W. Cai. Walk in the cloud: Learning curves for point clouds shape analysis. In *Proceedings of the IEEE International Conference on Computer Vision*, pages 895–904, 2021. Export Date: 31 July 2024; Cited By: 130. [2](#)
- [50] M. Xu, R. Ding, H. Zhao, and X. Qi. Paconv: Position adaptive convolution with dynamic kernel assembling on point clouds. In *Proceedings of the IEEE Computer Society Conference on Computer Vision and Pattern Recognition*, pages 3172–3181, 2021. Export Date: 31 July 2024; Cited By: 272.
- [51] M. Xu, J. Zhang, Z. Zhou, M. Xu, X. Qi, and Y. Qiao. Learning geometry-disentangled representation for complementary understanding of 3d object point cloud. In *35th AAAI Conference on Artificial Intelligence, AAAI 2021*, volume 4A, pages 3056–3064, 2021. Export Date: 31 July 2024; Cited By: 58. [2](#)
- [52] X. Xu, K. D. D. Willis, J. G. Lambourne, C. Y. Cheng, P. K. Jayaraman, and Y. Furukawa. Skexgen: Autoregressive generation of cad construction sequences with disentangled codebooks. In *Proceedings of Machine Learning Research*, volume 162, pages 24698–24724, 2022. Export Date: 23 July 2024; Cited By: 15. [3](#)
- [53] Y. Xu, T. Fan, M. Xu, L. Zeng, and Y. Qiao. Spidercnn: Deep learning on point sets with parameterized convolutional filters. In *Lecture Notes in Computer Science (including subseries Lecture Notes in Artificial Intelligence and Lecture Notes in Bioinformatics)*, volume 11212 LNCS, pages 90–105, 2018. Export Date: 08 October 2024; Cited By: 139. [2](#), [8](#)
- [54] Z. Yang and L. Wang. Learning relationships for multi-view 3d object recognition. In *Proceedings of the IEEE International Conference on Computer Vision*, volume 2019-October, pages 7504–7513, 2019. Export Date: 31 July 2024; Cited By: 125. [2](#)
- [55] T. Yu, J. Meng, and J. Yuan. Multi-view harmonized bilinear network for 3d object recognition. In *Proceedings of the IEEE Computer Society Conference on Computer Vision and Pattern Recognition*, pages 186–194, 2018. Export Date: 31 July 2024; Cited By: 240. [2](#)
- [56] Long Zeng, Zhi-kai Dong, Jia-yi Yu, Jun Hong, and Hong-yu Wang. Sketch-based retrieval and instantiation of parametric parts. *Computer-Aided Design*, 113:82–95, Aug. 2019. [3](#)
- [57] Long Zeng, Yong-Jin Liu, Sang Hun Lee, and Matthew Ming-Fai Yuen. Q-complex: Efficient non-manifold boundary representation with inclusion topology. *Computer-Aided Design*, 44(11):1115–1126, Nov. 2012. [1](#)
- [58] Long Zeng, Wei Jie Lv, Xin Yu Zhang, and Yong Jin Liu. Parametricnet: 6dof pose estimation network for parametric shapes in stacked scenarios. In *2021 IEEE International Conference on Robotics and Automation (ICRA)*, page 772–778. IEEE, May 2021. [2](#)
- [59] Z. Zhang, B. S. Hua, and S. K. Yeung. Shellnet: Efficient point cloud convolutional neural networks using concentric shells statistics. In *Proceedings of the IEEE International Conference on Computer Vision*, volume 2019-October, pages 1607–1616, 2019. Export Date: 31 July 2024; Cited By: 313.
- [60] H. Zhao, L. Jiang, J. Jia, P. Torr, and V. Koltun. Point transformer. In *Proceedings of the IEEE International Conference on Computer Vision*, pages 16239–16248, 2021. Export Date: 31 July 2024; Cited By: 927. [2](#)
- [61] S. Zhou, T. Tang, and B. Zhou. Cadparser: A learning approach of sequence modeling for b-rep cad. In *IJCAI International Joint Conference on Artificial Intelligence*, volume 2023-August, pages 1804–1812, 2023. Export Date: 23 July 2024; Cited By: 0. [2](#)

Constraint Learning for Parametric Point Cloud

Supplementary Material

A. Overview

This supplementary material provides additional details that supplement the main paper and includes more experimental results.

In Sec. B, we present the details of network architecture and data preparation in validation experiments. In Sec. D, we show more details of our constraint representation and constraint learning methods. In Sec. C, we provide the data construction and static of Parametric 20000 dataset. Finally, Sec. E offers data process for visualization and more results of experiments.

B. Validation Experiment

B.1. Constrain Expression

This section introduces the constraint expression in the validation experiments.

The constraint expression in validation experiments is defined in a simple manner: for a point, its constraint is defined by the relationship between the plane it attached and the reference plane, as shown in Fig. 10. This calculation process is carried out by openCASCADE Technology (OCCT). The constraint is represented in a one-hot encoding, where $(1, 0, 0)$ indicates perpendicular, $(0, 1, 0)$ indicates parallel, and $(0, 0, 1)$ indicates other constraints. Each point in the point cloud is expressed as $(Coordinate, constraint)$. For example, if the coordinate of a point is $(0.1, 0.2, 0.3)$, and the plane it attached is perpendicular to the reference plane, it is expressed as $(0.1, 0.2, 0.3, 1, 0, 0)$, where $(0.1, 0.2, 0.3)$ represents the point's coordinate, and $(1, 0, 0)$ denotes the type of constraint.

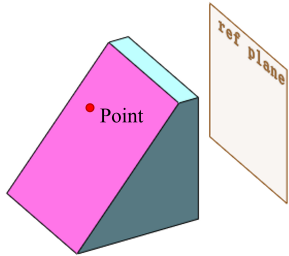


Figure 10. **Constraint expression in validation experiments.** The red point's constraint is expressed as the constraint type between the magenta plane and the reference plane, using one-hot encoding.

B.2. Dataset Generation

This section introduces the dataset generation procedures in the validation experiments.

The dataset generation for the validation experiments consists of the following steps:

1. Building the parametric templates for cuboids and prisms (with angles of $50^\circ, 60^\circ, 70^\circ, 80^\circ, 82^\circ, 85^\circ, 87^\circ, 89^\circ$). Afterwards determining the dimension range for each parameter. The parametric templates and the dimensions are shown in Fig. 11.
2. Assigning random values to the parameters in parametric templates. Each parametric template is instantiated into 5,000 B-Rep format CAD shapes, which are stored in STEP files [32].
3. Using OCCT to read the STEP files and convert them into meshes. Poisson disk sampling is then applied to sample points from meshes.
4. For the sampled points, OCCT is used to calculate the plane to which each point is attached. The constraint type for each point is then determined based on the relationship between the attached plane and the reference plane.
5. Rotating the generated point clouds randomly along the XYZ axes, within a range of $[-25^\circ, 25^\circ]$.
6. Assigning the generated point clouds to each experiments. The validation experiments involve binary classification of cuboids and prisms with specific angles. The point clouds used in each of the eight experiments are as follows (80 % for training, and 20 % for testing):

- Experiment 1: Cuboid \times 5000, Prism $50^\circ \times$ 5000
- Experiment 2: Cuboid \times 5000, Prism $60^\circ \times$ 5000
- Experiment 3: Cuboid \times 5000, Prism $70^\circ \times$ 5000
- Experiment 4: Cuboid \times 5000, Prism $80^\circ \times$ 5000
- Experiment 5: Cuboid \times 5000, Prism $82^\circ \times$ 5000
- Experiment 6: Cuboid \times 5000, Prism $85^\circ \times$ 5000
- Experiment 7: Cuboid \times 5000, Prism $87^\circ \times$ 5000
- Experiment 8: Cuboid \times 5000, Prism $89^\circ \times$ 5000

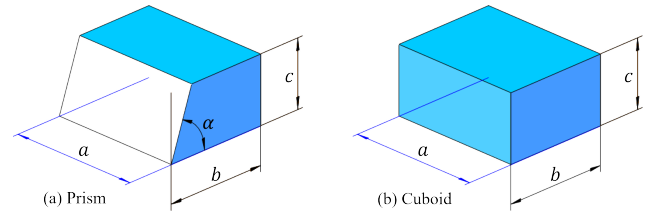


Figure 11. **Parametric templates for prisms and cuboids.** $a, b, c \in [0.3, 2.3]$, for prisms: $b > \frac{c}{\tan \alpha}$.

B.3. Model Design

This section introduces the structure of the constraint-aware model used in the validation experiments.

The constraint-aware model first employs a PointNet++ [34] backbone to predict point-wise constraints. These constraints are then concatenated with the point coordinates and passed through another PointNet++ backbone to determine the point cloud category. The model’s loss function is the sum of the classification loss and the constraint loss, as shown in Fig. 12

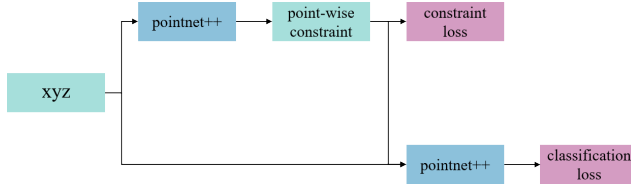


Figure 12. Constraint-aware model structure.

C. Parametric 20000 Dataset

C.1. Dataset Construction

This section provide details of purification process and data acquisition of Parametric 20000 dataset.

Purification: The purification process involved removing broken, duplicated, or overly complex CAD shapes requiring more than 4,000 points for point cloud representation.

Point cloud: The point cloud data in Parametric 20000 dataset containing about 2,200 points, point constraints is also included, each point is expressed as (Coordinate, Primitive Type, Main Axis Direction, Adjacency), the meshes and point clouds are generated from B-Rep data.

C.2. Dataset Statics

This section presents the shapes count and proportion statistics for each category in the Parametric 20000 dataset. Additionally, shapes from each category are showcased.

Parametric 20000 dataset is divided into 80 % for training and 20 % for testing.

The class distribution is shown in Fig. 13.

The proportion of shapes in each category are shown in Fig. 14.

Shapes instantiated from the parametric templates designed by our team names begin with "Num".

Example shapes from each category are shown in Fig. 15.

D. Constraint Learning Method Details

D.1. Defects of General Constraint Representation

The simple constraint expression in validation experiments is insufficient for a comprehensive definition, as selecting an appropriate reference plane for complex CAD shapes is challenging. Moreover, traditional constraint representations suffer from non-uniqueness, as shown in Fig. 16, defining the relations between three planes involves multiple constraint options, therefore, this approach is not well-suited for deep learning models.

The constraint is defined as a graph representation in some circumstances, where each node represents a primitive, and the edge between nodes represent their constraints. However, this approach is not well-suited for point cloud analysis. First, in cases where only point clouds are provided as input, the number of primitives is hard to obtain. Second, due to the unordered nature of point cloud, it is difficult to associate points with the corresponding primitives, making label design very challenging. Additionally, the graph representation essentially records the constraint relationships between each pair of primitives, for the CAD shapes contain many primitives, recording the relative positions between every pair of primitives would result in an overwhelming amount of data, making the expression of these relative positions impractical.

D.2. Constraint Representation

This section provides the process of Main Axis Direction and example constraint representation.

The main axis direction is processed to ensure its uniqueness, as one axis can determine two unit vectors with opposite direction. For a given axis, we first randomly select one of the two vectors, denoted as $v(x, y, z)$, and then process it using the following algorithm:

Data: Unit vector $v(x, y, z)$
Result: Unit vector after direction unification

```

1 if  $z < 0$  then
2    $v = -1 \times v;$ 
3   Return  $v;$ 
4 else if  $z == 0$  then
5   if  $y < 0$  then
6      $v = -1 \times v;$ 
7     Return  $v;$ 
8   else if  $y == 0$  then
9     if  $x < 0$  then
10       $v = -1 \times v;$ 
11      Return  $v;$ 
12 return  $v$ 
  
```

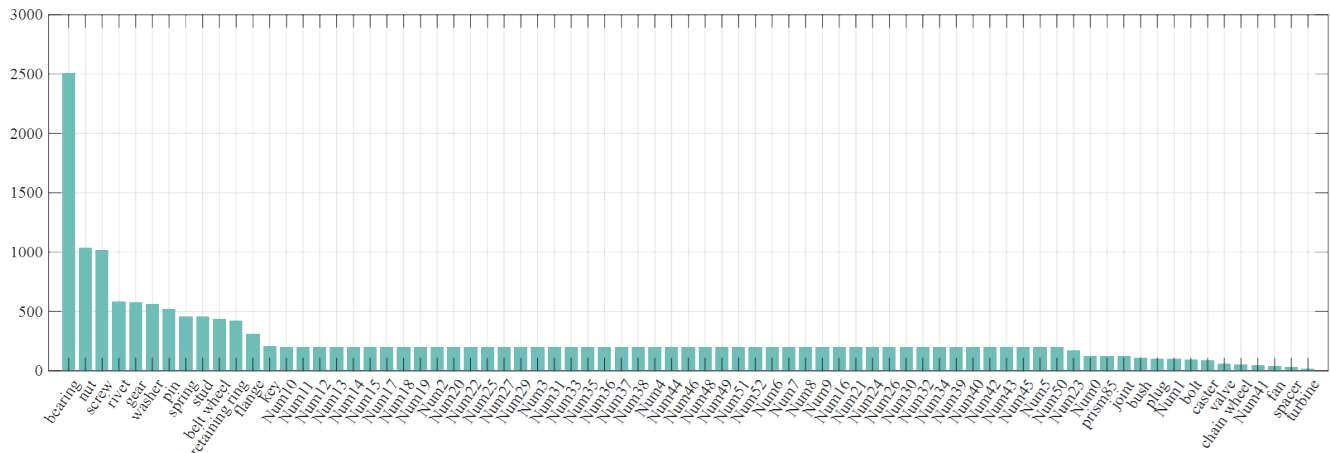


Figure 13. Quantity distribution of Parametric 20000 dataset.

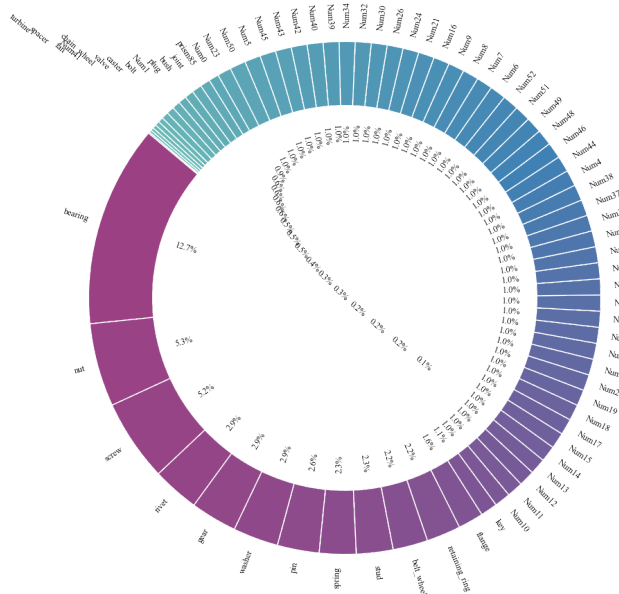


Figure 14. **Shapes proportion of Parametric 20000 dataset.**

A point with constraint is expressed as Fig. 17.

D.3. CST-BRep Module

This section explains why it is necessary to compute valid edges in the CST-BRep module.

The CST-BRep module is used to compute constraints from B-Rep data, and the computation process consists of the following steps:

Step 1: Point cloud generation (optional).

Step 2: Calculation of valid edges and the distance from each point to these valid edges. If the minimum distance is below a threshold, the point is classified as a edge-near point.

Step 3: Calculation of the primitives to which each point

attached, followed by analysis to determine point's Primitive Type and the Main Axis Direction.

In **Step 2**, valid edges are computed, as this helps to reduce the potential for data to mislead the deep learning model. The definition of valid edge is illustrated in Fig. 18. This definition is based on the observation that a complete cylinder in the B-Rep data stored in STEP files is often split into two half-cylinder faces. As a result, two generatrices form edges on the cylindrical surface, but the deep learning model cannot predict these edges, as shown in Fig. 19. Furthermore, in other cases, edges corresponding to smoothly connected faces are also difficult to identify, leading to confusion for deep learning models.

D.4. CST-PCD Module

This section provides a detailed explanation of the valid points in the computational steps that inspire the design of the CST-PCD Module.

The CST-PCD Module is used to predict constraints from point clouds. The design of the CST-PCD Module is inspired by the following calculation process:

For a point p in point cloud, its constraint could be calculated by the following steps:

1. Identify neighbor points around p .
2. From all neighbor points, identify those that belong to the same primitive as p ; these points are referred to as valid points.
3. Fit shapes such as cylinders or planes using valid points, and determine the primitive type with the smallest fitting error.
4. Based on the valid points and the primitive type, calculate the main axis direction and assess whether the point is near an edge.

In these steps, it is necessary to compute the valid points. We define the valid point as the neighbors that lie on the same primitive as the center point p , as visualized in Fig. 20.

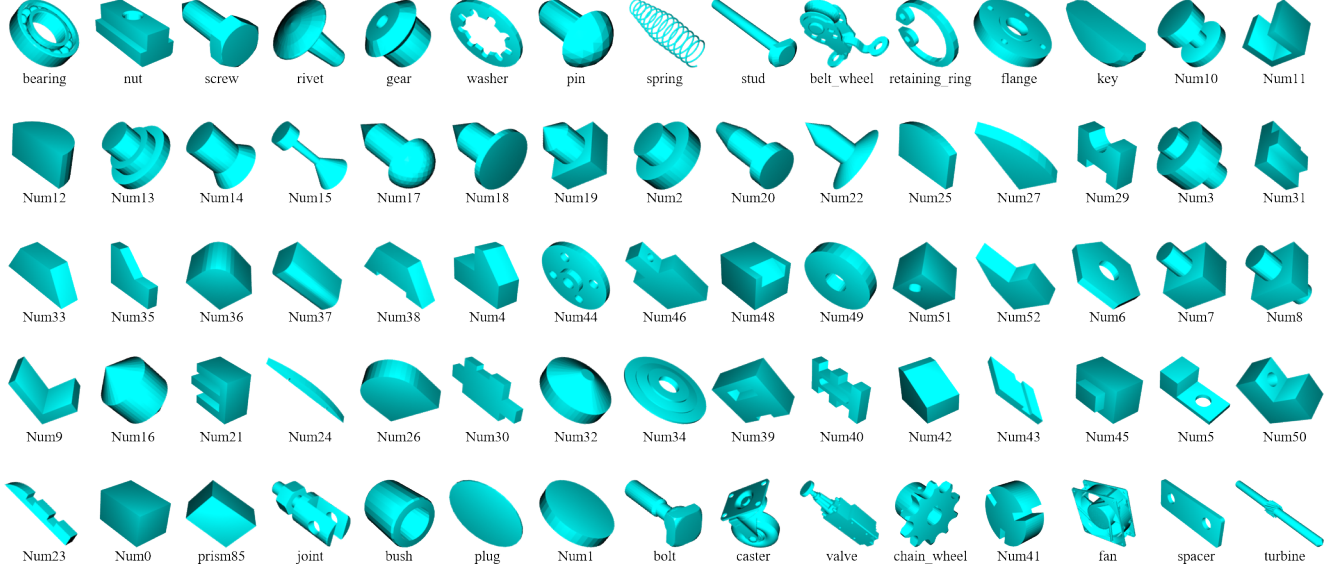


Figure 15. Example shapes for each category in Parametric 20000 dataset.

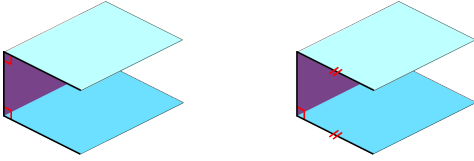


Figure 16. **Non-uniqueness of traditional constraint expression.** Left: Double vertical constraints, right: Vertical and parallel constraints.

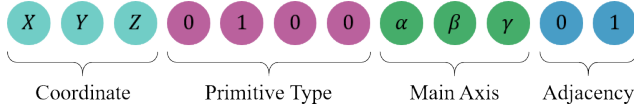


Figure 17. Expression of a point with constraint.

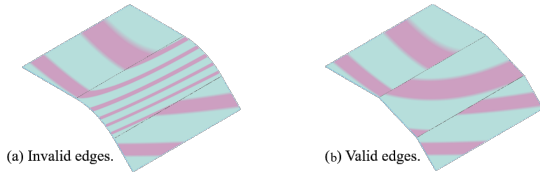


Figure 18. **Zebra stripes of primitives corresponding to invalid and valid edges.** Left: G1 or higher continuous at the invalid edges, right: G0 continuous at the valid edges.

These valid points can be used to determine whether the center point is near an edge, as well as to calculate the main axis direction and primitive type of the attached primitive, while the invalid points do not contribute to these calculations.

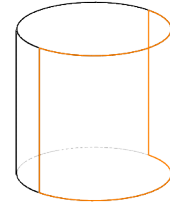


Figure 19. **Cylinder in B-Rep representation.** A complete cylindrical surface is represented as a combination of two half-cylinder surface, resulting in edges along the generatrices that cannot be recognized, thereby causing confusion for deep learning model.

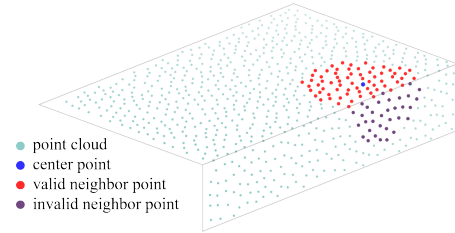


Figure 20. **Valid and invalid points for constraint calculation.**

D.5. SurfaceKNN

This section introduces the algorithm of SurfaceKNN.

SurfaceKNN based on the assumption that when KNN is applied with a small number of neighbors, the output points are searched along the shape's surface. This assumption has been validated in most cases. Leveraging this assumption, SurfaceKNN is accomplished by applying KNN with small number of neighbors iteratively. During each iteration, KNN is used to search a small set of neighbor-

ing points, which then serve as new central points for subsequent searches. This process continues until the desired number of points is obtained, as illustrated in Fig. 21.

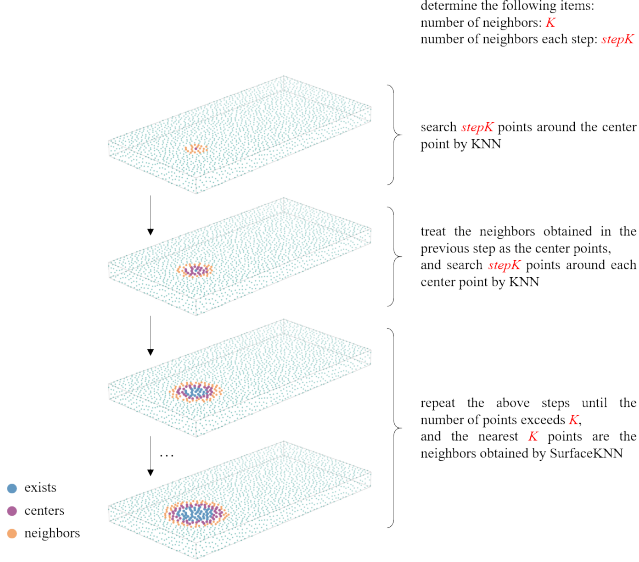


Figure 21. Algorithm of SurfaceKNN.

E. Classification Segmentation Experiments

E.1. Process to Visualize Main Axis Direction

The main axis direction of a point, denoted as $v = (x, y, z)$, is visualized as $R = \frac{x+1}{2}$, $G = \frac{y+1}{2}$, and $B = \frac{z+1}{2}$. Since the main axis direction is represented as a unit vector, $-1 \leq x, y, z \leq 1$, which results in $0 \leq \frac{x+1}{2}, \frac{y+1}{2}, \frac{z+1}{2} \leq 1$.

E.2. Constraint Visualization of CST-BRep

More constraints extracted by the CST-BRep module from the B-Rep are visualized in Fig. 22.

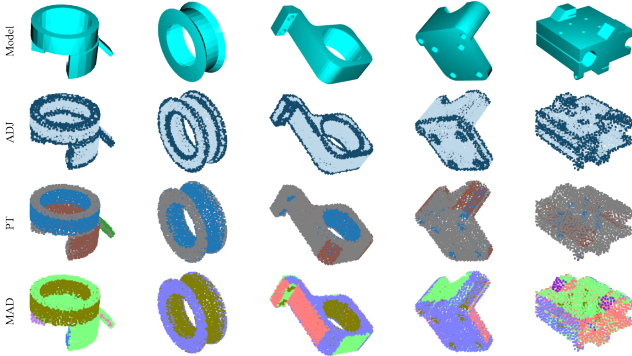
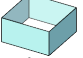
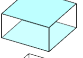
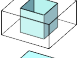

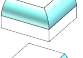
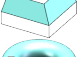

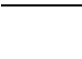


Figure 22. More constraint extraction results from the B-Rep data. ADJ: Adjacency, PT: Primitive Type, MAD: Main Axis Direction.

Table 6. **Part Segmentation Results on 360 Gallery.** OA: overall accuracy %. mIoU: instance mIoU %. mIoU*: class mIoU %. Segmentation categories from left to right are: Extrude Side, Extrude End, Cut Side, Cut End, Fillet, Chamfer, Revolve Side, Revolve End. PN: PointNet [33]. PN2: PointNet++ [34]. DGN: DGCNN [42]. 3DN: 3DGCN [26].

Method	PN	PN2	DGN	3DN	Ours
OA	42.13	58.18	64.02	60.58	70.76
mIoU	18.89	26.98	35.54	33.03	46.65
mIoU*	7.04	11.27	14.36	12.23	20.51
	19.83	49.80	54.48	50.67	61.29
	36.47	40.36	50.82	47.20	60.65
	0	0	0	0	0
	0	0	0	0	0
	0	0	0	0	0
	0	0	0	0	0
	0	0	9.60	0	0
	0	0	0	0	0

E.3. Segmentation

The full segmentation results of investigated methods on 360 gallery are shown in Tab. 6.